Proceedings of the 21st ICSMGE, Vienna, Austria, 14 – 19 June 2026. Pistrol, Adam & Schweiger (eds.)
Published by: ÖGG, Austrian Society for Geomechanics, Salzburg, Austria, ISBN 978-3-9503898-4-5
https://doi.org/10.53243/ICSMGE2026-2338

Softening behavior of volcanic ash soil containing Aso-4 pyroclastic flow deposits under cyclic loading

Kotori Kakazu, Takayuki Yamashita
Graduate School of Science and Technology, Kumamoto university, Kumamoto, Japan

Toshifumi Mukunoki
Faculty of Advanced Science and Technology, Kumamoto university, Kumamoto, Japan, mukunoki@kumamoto-u.ac.jp

ABSTRACT: The volcanic ash with cohesive soils (VACS) were observed from the significantly damaged ground deformations, including tilting of buildings and utility poles, as well as ground subsidence at Kumamoto Earthquake in 2016. It has been suggested that these ground deformations were potentially caused by the characteristics of the cohesive soils or other ground materials with anisotropic stress condition. VACS observed in the affected area exhibits a wide range of particle sizes, consisting of coarse fractions with crushable particles and fine fractions dominated by clay minerals such as halloysite. This type of soil is categorized as Aso-4, in Japan. On microscopic scale, the failure mechanism of Aso-4 remains unclear, particularly regarding how each soil component contributes to its softening, making this a key research challenge. To address this issue, this study aims to evaluate the softening characteristics of VACS by focusing on the sandy fraction through cyclic undrained triaxial tests with anisotropic stress condition. These tests were conducted on the sandy fraction of VACS sampled in Koshi, Kumamoto, derived from Aso-4 pyroclastic flow deposits, as well as on silica sand adjusted to the same particle size distribution. The results revealed that although little significant differences in liquefaction strength were observed, differences in axial strain and excess pore water pressure behavior were confirmed. The sandy fraction of VACS exhibited behavior more similar to the softening characteristics of clay rather than the liquefaction behavior of silica sand. To further investigate the internal structure of VACS, core sample were extracted from test specimen before and after performing cyclic undrained triaxial tests for X-ray CT imaging. The X-ray CT image indicated structural changes and primarily a reduction in voids were observed before and after softening.

KEYWORDS: Cyclic undrained triaxial test, Pyroclastic flow deposits, Softening.

1 INTRODUCTION

In 2016, the Kumamoto earthquake occurred with a magnitude of 7.3 and a maximum seismic intensity of 7, centered in Kumamoto prefecture in Kyushu, Japan. It began with a foreshock measuring a magnitude of 6.5, followed by the main shock with a magnitude of 7.3 in 28 hours. These two earthquakes were triggered by the strike-slip behavior of the closely located Futagawa and Hinagu fault zones (Mukunoki et al. 2016a). Mount Aso, an active volcano located in Kumamoto, has long contributed to the formation of volcanic soils across the Kyushu region and so volcanic ash with cohesive soil (VACS) are widely distributed in Kyushu, especially Kumamoto. In Mashiki town, located in the central part of Kumamoto prefecture, several types of damage were observed, including the tilting of buildings and the tilting or subsidence of utility poles. It has been pointed out that ground deformation due to cohesive soils and other soil types may have occurred as a result of the earthquake in this area. Especially, VACS formed by the eruption of Mt. Aso approximately 90,000 years ago is categorized Aso-4. When these pyroclastic flow deposits do not undergo welding and instead become clay-like through weathering and softening. The characteristics of the cohesive soils or other ground materials potentially caused severe ground deformations with anisotropic stress condition. Numerous reports have documented severe damage to both transportation infrastructure and buildings caused by the earthquake (Bhattacharya et al. 2018; Kiyota et al. 2016; Goda et al. 2016).

The objective of this study is to clarify the characteristics of VACS under cyclic loading, focusing on its sandy fraction. Since the sandy fraction forming the skeletal structure of VACS is derived from pyroclastic flow deposits, it consists of mineral, volcanic glass, and porous pumice (Yamashita et al. 2024). For this reason, it significantly differs from ordinary sand in terms of particle shape and uniformity of particle strength. We expected that the liquefaction strength may be lower than that of standard sand due to these effects. To investigate this, we compared the strength difference with silica sand using liquefaction curves and attempted to quantitatively evaluate strength. In this study, we focused on particle fragility and evaluated the softening characteristics of the sandy fraction in VACS, which is formed pyroclastic flow deposits of Mt Aso, by conducting cyclic undrained triaxial tests. In consideration of the deformations observed in the foundation ground of residential buildings during the 2016 Kumamoto Earthquake, a vertical overburden pressure was applied to the specimens in order to simulate an anisotropic stress condition for the experiments.

2 METHODS

The VACS used in the experiments was collected from Koshi city, Kumamoto prefecture. The physical properties of tested soil are shown in Table 1 and its grain size distribution curves are shown in Figure 1. The specimen was the sandy fraction of VACS, obtained by washing out particles smaller than 75 μm based on the grain size distribution curve in Figure 1. For comparison of cyclic loading behavior, samples were also prepared using silica sand No. 3, No. 5, and No. 7, adjusted to match the same passing mass percentage as the sandy fraction of VACS. The physical properties of these samples are summarized in Table 2.

To evaluate the softening characteristics of both sandy fraction of VACS and silica sand, cyclic undrained loading tests were conducted. The tests were used uniform amplitude loading under stress control. The test conditions are listed in Table 3. The specimens were cylindrical, with a diameter of 50 mm and a height of 100 mm, and were prepared by the air pluviation method to achieve a target relative density of Dr =60%. The

Table 1. Physical properties of the VACS.

Plastic limit PL (%)	Liquid limit LL(%)	Plasticity index IP	Average particle diameter D_{50}(mm)	Soil particle density (g/cm^3)
37.57	64.44	26.87	0.015	2.569

Table 2. Physical properties of sand.

Sample	Sandy fraction of VACS	Silica sand
Soil particle density (g/cm^3)	2.826	2.651
Maximum void ratio	1.51	1.03
Minimum void ratio	0.945	0.606
Average particle diameter D_{50}(mm)	0.22	0.22

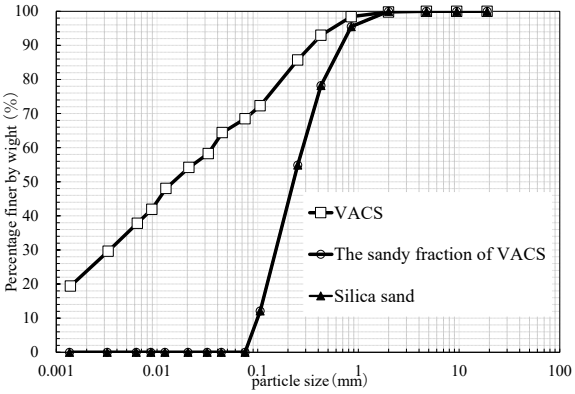

Figure 1. Grain size distribution curves.

Table 3. The conditions of the experiment.

No.	1	2	3	4
Sample	Sandy fraction of VACS			
Frequency (Hz)	0.1			
Effective confining pressure (kPa)	100			
Relative density *Dr* (%)	57.8	65.7	54.8	59.9
Dry density after consolidation ρ_d (g/cm^3)	1.295	1.322	1.285	1.302
Cyclic stress ratio	0.243	0.194	0.170	0.158
No.	5	6	7	8
Sample	Silica sand			
Frequency (Hz)	0.1			
Effective confining pressure (kPa)	100			
Relative density *Dr* (%)	64.0	64.5	65.3	64.0
Dry density after consolidation ρ_d (g/cm^3)	1.508	1.510	1.513	1.508
Cyclic stress ratio	0.243	0.194	0.170	0.158

specimens were then saturated using de-air water, and saturation was confirmed with a B-value of 0.95 or higher. Subsequently, anisotropic consolidation was achieved by first applying a deviator stress corresponding to 15% of the effective confining pressure under undrained conditions, and then switching to drained conditions. As a result, anisotropic consolidation was established at a confining pressure of 100 kPa and a vertical stress of 115 kPa. Hence, the mean effective principal stress σ_0' was 105 kPa. Finally, cyclic loading was applied under undrained conditions using a 0.1 Hz sine wave.

3 RESULTS

3.1 Comparison of Excess Pore Water Pressure and Axial Strain in Cyclic Undrained Triaxial Tests

Figure 2 shows the maximum excess pore water pressure ratio and double amplitude of axial strain (DA) obtained at each cycle under cyclic stress ratios of $R = \sigma_d/2\sigma_0$'=0.158 and 0.170.

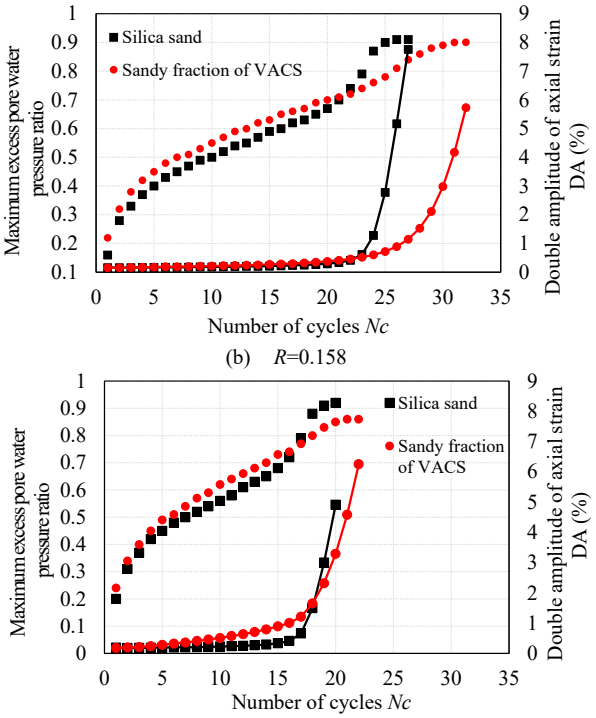

Figure 2. Relationship between the number of loading cycles, the maximum excess pore water pressure ratio, and the double amplitude axial strain.

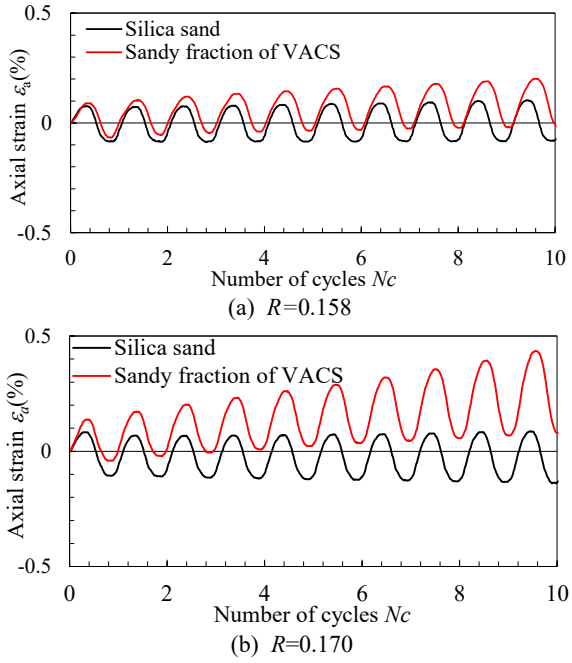

Figure 3. Relationship between the number of loading cycles and axial strain (up to *Nc* = 10).

The vertical axis shows the maximum excess pore water pressure ratio and DA, while the horizontal axis shows the number of cycles *Nc* until the DA reaches 5%. First, the transition of the maximum excess pore water pressure ratio is compared. For silica sand, the increase becomes pronounced around *Nc*=22 at *R*=0.158, and around *Nc*=16 at *R*=0.170. Corresponding to these changes, a notable increase in DA is also observed. In contrast, for the sandy fraction of VACS, no

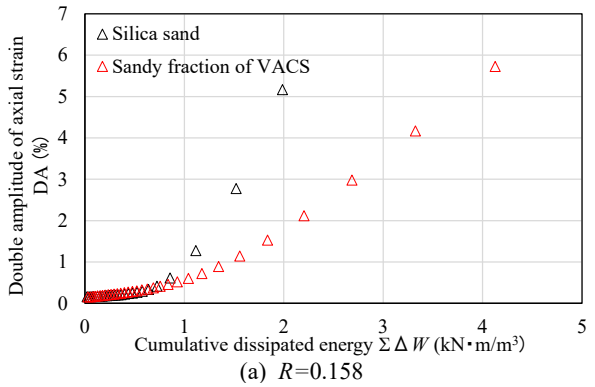

(a) R=0.158

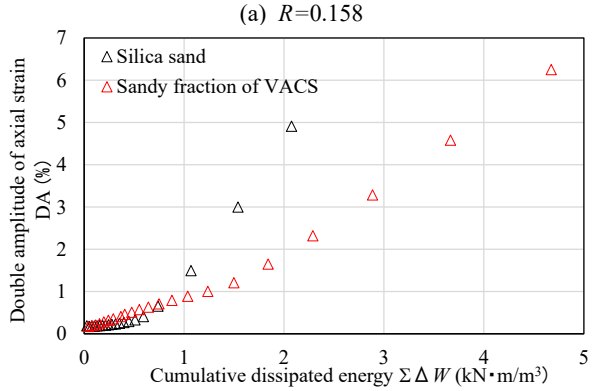

(b) R=0.170

Figure 4. Relationship between cumulative dissipated energy (ΣΔW) and double amplitude axial strain.

clear inflection points were seen, and the excess pore water pressure tended to increase more gradually.

Next, comparing the maximum excess pore water pressure ratio at the cycle in which DA reaches 5% across all test cases, silica sand showed values of 0.90-0.92, while the sandy fraction of VACS showed slightly lower values of 0.86-0.90. These results suggested that silica sand undergoes typical liquefaction behavior, characterized by a reduction in effective stress between particles due to the buildup of excess pore water pressure.

On the other hand, the sandy fraction of VACS reached the softening indicator of DA=5% in this paper even before a significant increase in excess pore water pressure, indicating that the specimen softened prior to full pore water pressure buildup. This implies that the sandy fraction of VACS undergoes softening via a different mechanism than silica sand.

Next, Figure 3 shows the relationship between axial strain and the number of cycles up to N_c=10. For silica sand, axial strain responds almost symmetrically in both compression and extension directions. However, the sandy fraction of VACS shows a tendency for axial strain to accumulate mainly on the compression side from the early stages of loading. This difference in deformation behavior suggests that, in the early stages of loading, silica sand exhibits elastic behavior, whereas the sandy fraction of VACS behaves plastically.

3.2 Comparison of dissipated energy

Figure 4 shows the relationship between cumulative dissipated energy ($\sum \Delta W$) and double amplitude of axial strain (DA). $\sum \Delta W$ calculated from the area enclosed by the stress-strain hysteresis loops, reflects the energy dissipated due to damage, friction and other factors during cyclic loading (Sun et al. 2025; Zavala et al. 2024). Figure 4 clearly shows that the sandy fraction of VACS exhibits a higher cumulative energy input than silica sand at the same level of double amplitude (DA), particularly when comparing the last three data points for silica

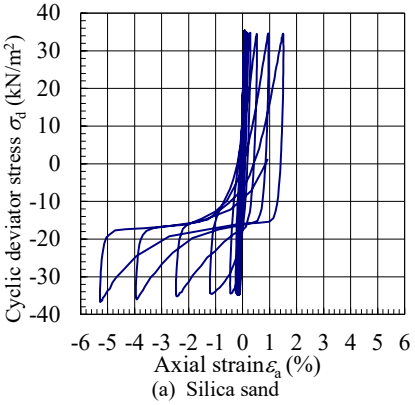

(a) Silica sand

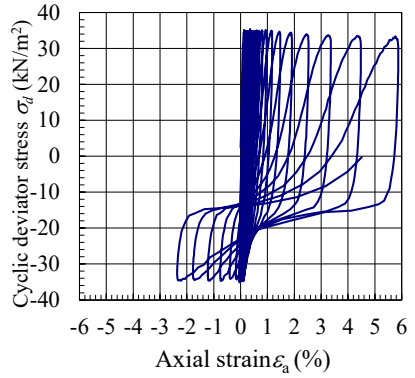

(b) Sandy fraction of VACS

Figure 5. Shape of hysteresis curves for the silica sand and the sandy fraction of VACS (R = 0.170).

sand. This result suggests that plastic deformation occurs in the sandy fraction of VACS greater than silica sand's case, leading to increased energy dissipation during cyclic loading. Furthermore, for the same cumulative dissipated energy input, the DA of the VACS sandy fraction is smaller than DA of silica sand, indicating its higher energy absorption efficiency under deformation. This implies that more strain energy is required to reach the same level of deformation and that this energy remains as residual strain in the material. A larger amount of absorbed energy before reaching DA=5% indicates that the material processes a certain degree of toughness against strength degradation. While the sandy fraction of VACS can be considered to exhibit relatively high toughness, it is also inferred that notable plastic deformation occurs during loading, such as rearrangement of soil particles, which affects the internal structure of the soil. Additionally, from Figure 2, there is no significant difference between the sandy fraction of VACS and silica sand in terms of the number of cycles required to reach DA =5%.

Compared to silica sand, the sandy fraction of VACS exhibits a larger cumulative energy input ($\sum \Delta W$) at the same level of DA, indicating that more strain energy is consumed to reach the same amount of deformation. This suggests that strain accumulates within the specimen, leading to structural changes in the soil and, consequently, a reduction in stiffness. While the sandy fraction of VACS specimen undergoes ductile failure by absorbing energy, the behavior is not necessarily indicative of toughness, but rather results in an increase in DA, as the energy is primarily consumed by deformation due to cyclic loading.

3.3 Comparison of stiffness in hysteresis curves

Figure 5 (a) and (b) shows the hysteresis curves of silica sand and the sandy fraction of VACS obtained under R=0.170. It was observed that the both hysteresis curves were shifted by -15 kN/m² because of applying anisotropic consolidation to the

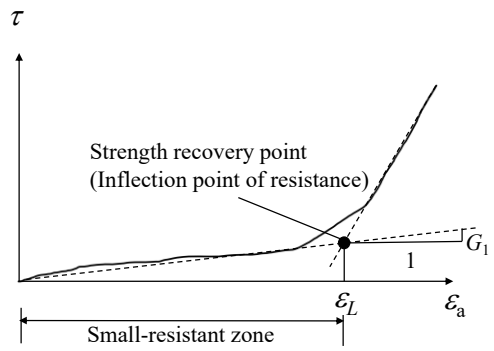

Figure 6. Modeling of shear stress–shear strain behavior.

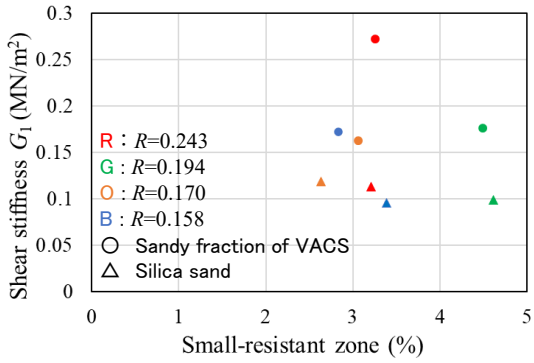

Figure 7. Comparison of shear stiffness and micro-resistance zone between sandy fraction of VACS and silica sand.

specimens. A comparison of the hysteresis curves of the two materials reveals that silica sand exhibits a strain response characterized by increased tensile strain and suppressed compressive strain. This behavior is indicative of cyclic mobility, in which apparent stiffness recovers when the effective stress is close to zero. In contrast, the hysteresis curve of the sandy fraction of VACS displays a different shape. The axial strain biased toward the compressive side, which is considered to be influenced by plastic deformation initiated during the early stages of loading. To compare the behavior after reaching DA=5%, Figure 6 presents a modeled shear stress-strain relationship after the DA=5% point (Yasuda et al. 2017). The secant sloop up to the strength recovery point (resistance infection point) is defined as G_1, and the small-resistant zone was also calculated. The small-resistant zone was defined as the strain range from the point where the strain rate exceeds 0.1% in 0.1 seconds to the resistance infection point, providing a quantitative measure of the liquefied state. Figure 7 compares the shear stiffness G_1 and small-resistant zone between the sandy fraction of VACS and silica sands. The results show less significant difference in the small-resistant zone, suggesting that the development of axial strain after reaching DA=5% is similar for both materials. However, for all stress ratios R, the shear stiffness G_1 of the sandy fraction of VACS is consistently greater than silica sand as shown in Figure 7. This result indicates that unlike silica sand where stiffness is recovered through changes in deviator stress, the sandy fraction of VACS retains a certain degree of stiffness even after deformation, indicating that the specimen's stiffness was not entirely lost.

Figure 8 shows a comparison of the particle size distribution curves before and after the cyclic loading at R=0.243. The percentage of particles passing 75 μm increased by 17.4%, suggesting that pumice particles within the 106-850 μm range fractured and became finer. This fragmentation likely generated fine particles that contributed to cohesion between

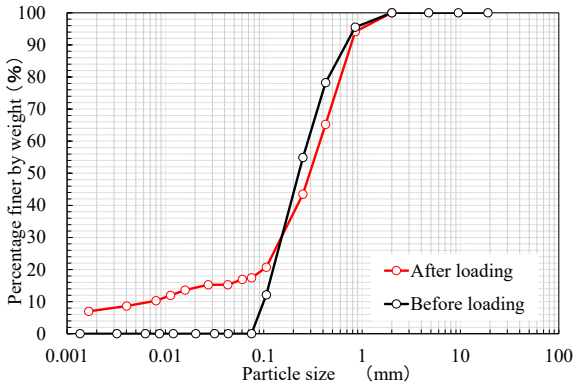

Figure 8. Grain size distribution curves before and after loading.

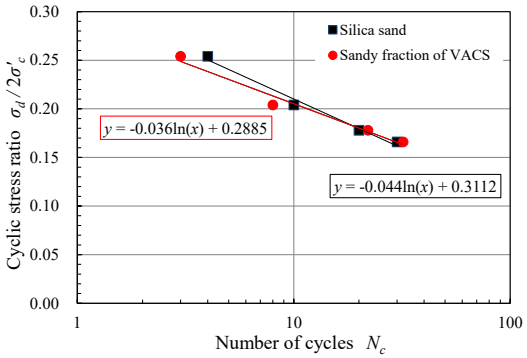

Figure 9. Liquefaction strength curves for the silica sand and the sandy fraction of VACS.

soil grains, thereby preserving some stiffness. Miura et al. (2003) reported that crushable volcanic soils exhibit contractive behavior under confining pressure of 49-392 kPa in triaxial tests, and that such contractive tendencies become more pronounced with increasing effective confining pressure and under drained conditions. Although the test in this study was conducted under an effective confining pressure of 100 kPa, particle crushing is likely to have occurred during either the consolidation stage or the subsequent cyclic loading phase, or possibly both.

Given that the dynamic behavior of the sandy fraction of VACS resembles that of clay due to the increased fine content the deformation mechanism is considered to be softening rather than liquefaction. Moreover, the previous study has reported that silica sand under high confining pressure undergoes particle crushing, exhibiting behavior similar to that observed in this study (Hyodo et al. 2002). For further information on the dynamic behavior of clay, please refer to the following Hyodo et al. (1994). Furthermore, the strength deduction is thought to be caused by both static loading during consolidation and cyclic loading thereafter.

3.4 Liquefaction strength curves

Figure 9 shows the liquefaction strength curves for the silica sand and sandy fraction of VACS specimens. There curves plot the number of loading cycles required to reach DA =5% for stress ratios R=0.243, 0.194, 0.170 and 0.158. There is little significant difference in the number of cycles needed to reach DA=5% between the sandy fraction of VACS and silica sand. The RL_{20}, representing the stress ratio to reach DA=5% during 20 cycles, are 0.180 for the sandy fraction of VACS and 0.176 for silica sand. This confirms that both materials reached loading cycles, or in other words, under equivalent loading energy. However, based on the previously discussed results, it is considered that the sandy fraction of VACS reached the

deformation level of DA=5% through a combination of strain accumulation due to plastic deformation and an increase in excess pore water pressure.

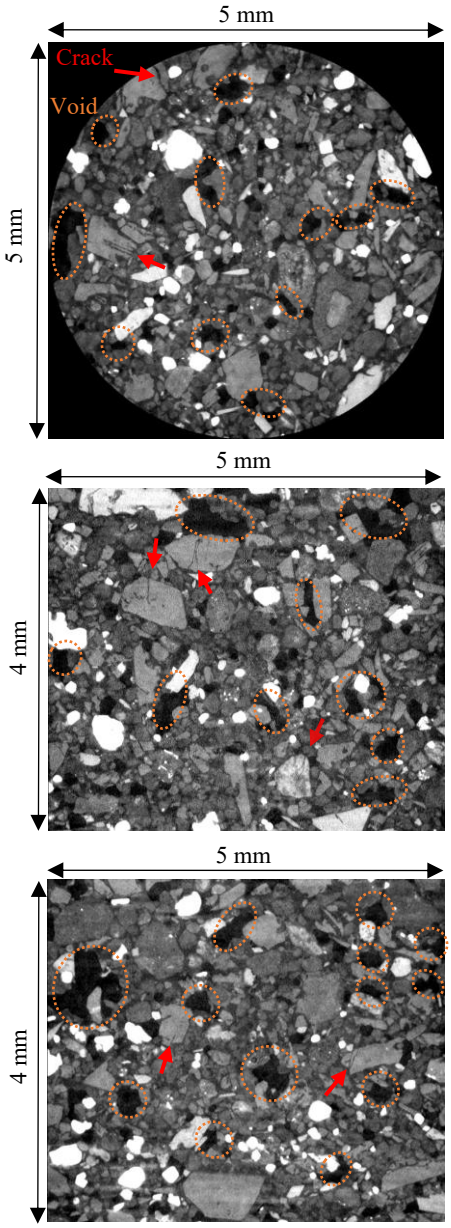

Top : horizontal slice (XY plane)
Middle: vertical slice (YZ plane)
Bottom: vertical slice (XZ plane))

Figure 10. CT images before consolidation.

Table 4. X-ray CT scan parameters.

Pixel size (μm)	5
Focus-to-center-distance (FCD, mm)	11
Number of accumulations	3
Integration time (ms)	499
Number of views	1667
Tube voltage (kV)	120
Tube current (μA)	100
Voxel dimensions	1024 × 1024 × 882

4 OBSERVATION IN VACS USING X-RAY CT

The micro-focused X-ray computed tomography (CT) scanner (TOSCANER-323000FPD, manufactured by Toshiba IT & Control System Corporation) at the X-Earth Center Kumamoto University was used to observe the difference in internal

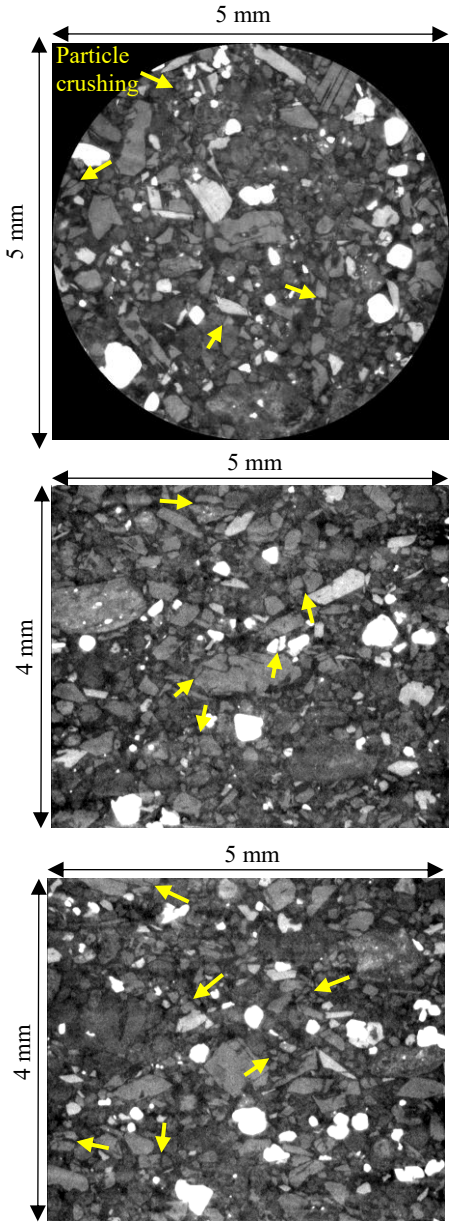

Top : horizontal slice (XY plane)
Middle: vertical slice (YZ axial)
Bottom: vertical slice (XZ axial)

Figure 11. CT images after consolidation and loading.

structure of the sandy fraction of VACS specimen before and after consolidation and loading. The scanning conditions are shown in Table 4. Sampling was conducted using a tube with an inner diameter of 10 mm, and the upper 2.5 cm of the specimen was scanned. It should be noted that, due to experimental setup limitations, the same specimen is not scanned twice, instead, a new specimen is reconstructed for the second scan after the initial sample had been scanned in its initial state. The first scan was conducted before consolidation, and the second scan after consolidation and loading. Following the loading process, the specimen was brought to a drained by allowing dissipation of excess porewater pressure, and sampling was performed thereafter. The primary advantage of X-ray CT scanning lies in its ability to non-destructively visualize the internal structure of soil. For research in soil

mechanics using X-ray CT, the reader is referred to Takano et al. (2015) and Hall et al. (2009).

Figure 10 and Figure 11 show X-ray CT images of the specimen sampled from tested specimen before and after softening, respectively. These include cross-sectional views in the XY, YZ, and XZ planes. X-ray CT images provide the internal density distribution of scanned specimens, expressed in 256 grayscale levels ranging from black (lowest density) to white (highest density). Usually, particle density in each size of particles is almost similar, however, particles of VACS have different particle density. Therefore, the white is the hardest minerals involving in VACS and the black should be void filled with water. In general, sand particles exhibit nearly uniform particle density regardless of their grain size (Mukunoki et al. 2016b). However, X-ray CT images of the sandy fraction of VACS reveal the presence of particles with higher brightness, suggesting variations in particle density among individual grains. This heterogeneity in particle density is considered a characteristic feature of the sandy fraction of VACS and may contribute to the variability in shear strength observed in laboratory shear tests.

In the CT image for before consolidation as shown in Figure10, several large voids can be observed, as indicated by the dashed circles. In contrast, after consolidation and cyclic loading as shown in Figure 11, voids seem to significantly reduced in size. Besides, highlights areas where particle breakage is estimated to have occurred. Even in CT images for before consolidation, cracks, as indicates by red arrows, can be observed in some particles. This suggests that volcanic ash particles are originally fragile, and that particle crushing and hence strength reduction could have already occurred during static compaction processes. To address this issue more clearly, a cyclic loading test using micro-focused X-ray CT is required. This approach would allow the tested specimen to be scanned, enabling a detailed discussion of the internal condition of the VACS material.

5 CONCLUSIONS

In this study, cyclic undrained triaxial tests were conducted focusing primarily the sandy fraction of volcanic ash with cohesive soil (VACS), in order to evaluate its softening characteristics. Additionally, comparisons were made with silica sand to highlight difference. The main findings of this study are summarized below:

1. The sandy fraction of VACS is characterized by softening occurring generally before the excess pore water pressure ratio reaches 0.90
2. The cumulative dissipated energy of the sandy fraction of VACS was greater than that of silica sand, suggesting that strain energy is consumed during the progression of plastic deformation.
3. Although there was no significant difference in the number of cycles required double amplitude of axial strain (DA)=5% between the sandy fraction of VACS and silica sand, plastic deformation associated with an increase in fine particles was observed in the sandy fraction of VACS. During progressing plastic deformation process, excess pore water pressure appeared to influence and accelerate deformation, potentially leading softening.
4. X-ray CT image of the sandy fraction of VACS specimen before and after softening revealed observable changes in internal structure.

As the next step, tests under isotropic stress conditions should be performed in order to compare the results with those obtained under anisotropic conditions.

6 ACKNOWLEDGEMENT

Authors would like to appreciate Associate Professor Kota Wakinaka of National Institute of Technology, Kumamoto College for his essential comments in the cyclic triaxial testing.

7 REFERENCES

Bhattacharya, S., Hyodo, M., Nikitas, G., Ismael, B., Suzuki, H., Lombardi, D., Egami, S., Watanabe, G. and Goda, K. 2018. Geotechnical and infrastructural damage due to the 2016 Kumamoto earthquake sequence. *Soil Dynamics and Earthquake Engineering*, 104, 390-394.

Goda, K., Campbell, G., Hulme, L., Ismael, B., Ke, L., Marsh, R., Sammonds, P., So, E., Okumura, Y., Kishi, N., Koyama, M., Yotsui, S., Kiyono, J., Wu, S. and Wilkinson, S. 2016. The 2016 Kumamoto Japan Earthquakes: Cascading Geological Hazards and Compounding Risks. *Frontiers in Built Environment*, 2, 19.

Hall, S.A., Lenoir, N., Viggiani, G., Desrues, J. and Bésuelle, P. 2009. Strain localisation in sand under triaxial loading: characterisation by X-ray micro tomography and 3D digital image correlation. *Proceedings of the 1st International Symposium on Computational Geomechanics (ComGeo I)*, Juan-les-Pins, Côte d'Azur, France.

Hyodo, M., Yamamoto, Y. and Sugiyama, M. 1994. Undrained cyclic shear behaviour of normally consolidated clay subjected to initial static shear stress. *Soils and Foundations*, 34(4), 1-11.

Hyodo, M., Hyde, A.F.L., Aramaki, N. and Nakata, Y. 2002. Undrained monotonic and cyclic shear behaviour of sand under low and high confining stresses. *Soils and Foundations*, 42(3), 63-76.

Kiyota, T., Ikeda, T., Konagai, K. and Shiga, M. 2017. Geotechnical Damage Caused by the 2016 Kumamoto Earthquake, Japan. *International Journal of Geoengineering Case Histories*, 4(2), 78-95.

Miura, S., Yagi, K. and Asonuma, T. 2003. Deformation-strength evaluation of crushable volcanic soils by laboratory and in-situ testing. *Soils and Foundations*, 43(4), 47-57.

Mukunoki, T., Kasama, K., Murakami, S., Ikemi, H., Ishikura, R., Fujikawa, T., Yasufuku, N., and Kitazono, Y. 2016a. Reconnaissance report on geotechnical damage caused by an earthquake with JMA seismic intensity 7 twice in 28h, Kumamoto, Japan, *Soils and Foundations*, 56(6), 947-964.

Mukunoki, T., Miyata, Y., Mikami, K., Shiota, E. 2016b. X-ray CT analysis of pore structure in sand, *Solid Earth*, 7, 929–942.

Sun, Y., Zhang, H., Liu, Y., Wu, K. and Zheng, Y. 2025. Characterization of the evolution of energy loss rate in cyclic load testing of marine soft soil. *Applied Sciences*, 15(5), 2354.

Takano, D., Lenoir, N., Otani, J. and Hall, S.A. 2015. Localised deformation in a wide-grained sand under triaxial compression revealed by X-ray tomography and digital image correlation. *Soils and Foundations*, 55(4), 906-915.

Yamashita, T., Shida, K., Yoshinaga, T., Hashimoto, A., and Mukunoki, T. 2024. Physical properties of the soft sections of the Aso-4 pyroclastic-flow and the Aso-4 co-ignimbrite ash-fall deposits. *Proceedings of the International Joint Symposium Surabaya Indonesia 2024, Multi-Mitigation of Geotechnical and Geoenvironmental Engineering to Natural Disaster on Problematic Soils*, 80-83.

Yasuda, S., Yoshida, N., Adachi, K., Kiku, H. and Ishikawa, K. 2017. Simplified evaluation method of liquefaction-induced residual displacement. *Journal of Japan Association for Earthquake Engineering*, 17(6), 1-20.

Zavala, J.G., Pando, A.M., Park, Y. and Aguilar, R. 2024. Assessment of dissipated energy-based failure criteria for sands under cyclic loading. *Proceedings of the 17th Pan-American Conference on Soil Mechanics and Geotechnical Engineering (XVII PCSMGE) and the 2nd Latin-American Regional Conference of the International Association for Engineering Geology and the Environment (IAEG),* La Serena, Chile.